On line estimation of rolling resistance for intelligent tires

N. Roveri[1], G. Pepe[1], A. Carcaterra[1]
[1] Department of Mechanics and Aeronautics, Sapienza , University of Rome,
Via Eudossiana, 18, 00184, Rome, Italy
e-mail: **nicola.roveri@gmail.com**

Abstract
The analysis of a rolling tire is a complex problem of nonlinear elasticity. Although in the technical literature some tire models have been presented, the phenomena involved in the tire rolling are far to be completely understood. In particular, small knowledge comes even from experimental direct observation of the rolling tire, in terms of dynamic contact patch, instantaneous dissipation due to rubber-road friction and hysteretic behavior of the tire structure, and instantaneous grip. This paper illustrates in details a new powerful technology that the research group has developed in the context of the project OPTYRE. A new wireless optical system based on Fiber Bragg Grating strain sensors permits a direct observation of the inner tire stress when rolling in real conditions on the road. From this information, following a new suitably developed tire model, it is possible to identify the instant area of the contact patch, the grip conditions as well the instant dissipation, which is the object of the present work.

1 Introduction

In efforts to reduce the greenhouse emissions increasing the efficiency of road vehicles is a fundamental task, since the automotive industry is one of the major responsible for greenhouse gases and electricity production [1]. One of the main sources of dissipation in road vehicles is tire rolling resistance, its contribution to the fuel consumption can amount up to 30%, depending on the drive cycle [2].

The rolling resistance is defined as the energy consumed per unit of distance travelled, and it is equivalent to a drag force. Tyres are made of reinforced rubber, which is a viscoelastic material, as a result the loading and unloading stiffness curves do not exactly coincide and part of the energy is dissipated as heat as the tire deforms. Hysteretic effects depend on the mechanical characteristics of the tire, for instance the dissipated energy decreases as temperature increases. Due to the wide range of demands that tires must perform, optimising tire design can be often a compromise: modern tires have to provide high level of grip, required for cornering, braking and accelerating and, more generally, to guarantee satisfactory handling abilities, while keeping the dissipated energy as low as possible. Understanding the phenomena that govern tire energy losses together with the experimental measure of the rolling resistance are two of the main tasks in the field of intelligent tire [3-14].

The development of an embedded sensor system for monitoring key variables, such as pressure, strain, temperature, acceleration, wheel loading, friction and tread wear, is a hard task and requires advanced technologies in the field of sensors and data transmission methods. Moreover, the design of data transmission and power supply systems are further challenging tasks [3, 4]. The use of tire as a sensor has been the focus of numerous research studies and patents in the last twenty years, with special attention to friction identification. Concerning indirect variable monitoring, the variable of interest is extrapolated from the sensed parameters, which are mainly vehicle velocity and wheel angular speed [15, 16], Due to nonlinear relationships [11, 12, 14] among tire parameters, quantitative relations are difficult to acquire and fuzzy logic controller [17] or Kalman filter [18] have been used. Even though indirect methods use existing sensors and are easy to install, their accuracy is low and a calibration is often required when one or more tires are substituted or when the pressure is adjusted [18].

Opposite to the indirect techniques, direct methods have higher accuracy; since the sensitivity is related to particle size, MEMS are suited for high-sensitivity pressure sensors [19] or to measure the tread deformation [20]. Regarding the rolling resistance, it is usually related to the vehicle velocity using empirical models [21], and, the Authors' knowledge, its on line measurements has not been carried out yet to.

Direct or indirect sensing methods only permit to acquire data with poor time and spatial accuracy, they are not able to sense and transmit high speed dynamic quantities [6]: more research is indeed required for better resolution. In spite of the technological advances, commercial transducers to measure directly the tire-road friction coefficient which can be adopted for applications are still not available. Recent advances in sensors and related electronics that allowed to gain accurate and real time estimation, produced further solutions opening the way to potential industrial products [3, 4, 9] as in the case of Cyber Tyre [4, 10].

In this context, the need of simple measurements together with the requirement of reliable identification processes [23-25] makes this field challenging, where new investigations and potential solutions are needed. This paper is part of a research project [3, 6, 9] focused on the development of a new system for the real-time identification of the tire stress during rolling and residual grip estimation. The paper is devoted on the real time identification of the rolling resistance, based on a new analytical model and which uses the tire strain acquired by the developed optical sensor apparatus embedded into the tire.

The organization of the paper is as follow. Section 2 presents the experimental apparatus developed and adopted for the test campaign. In section 3 the theoretical model of tire and the proposed algorithm for the estimation of the rolling resistance is presented. Theoretical results open the way for the experimental identification of the roiling resistance, as shown in section 4, where the signals acquired during the experimental test campaign are presented and the performance of the analytical model are tested. Finally, section 5 presents some perspectives of the work and draws some conclusions.

2 Layout of the OPTYRE system

As a quick reminder, Fiber Bragg Grating (FBG) based sensors are made recreating a spatially recurring alternation of the glass refraction index in a single mode optical fiber. The grating turns the fiber into an optical filter, in fact, a specifically narrowband infrared light fired into the fiber is reflected to a spectrum analyzer, while the rest of the light is fully transmitted.

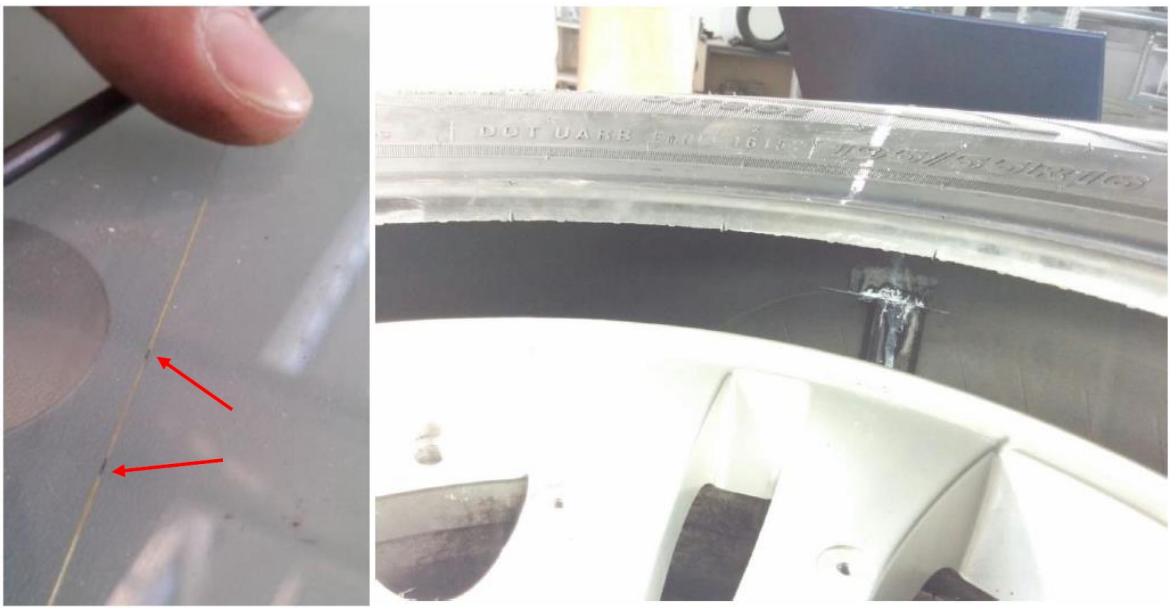

Figure 1: On the left, the optical fibre with one FBG, the sensor lies within the black marks on the line, on the right, the optical fiber pasted into the inner liner of the tire.

Therefore, a FBG sensor is a distributed Bragg reflector, i.e. a periodical variation of refractive index, inside the core of optical fiber, as in Fig. 1, able to reflect a particular wavelength of light and transmit all the others. The reflected Bragg wavelength λ_B is related to the refractive index of the fibre n and to the period of the refractive index modulation Λ by the formula: $\lambda_B=2n\Lambda$. Thus the FBG is a strain sensor which measures the local axial deformation of optical fibre.

The previous relationship implies that the reflected wavelength λ_B is modified by any variation in the physical or mechanical properties of the grating sensor. As an example, strain on the fibre alters Λ and *neff* through stress optic effect. Likewise, changes in temperature modifies *neff* via thermo-optic effects and, when the fibre is unconstrained, Λ is influenced by thermal variations. These phenomena are enlightened in eq. (1), where the first term on the right hand side gives the effect of strain on λ_B and the second describes the influence of temperature.

These perturbations can be determined by monitoring the wavelength change of the FBG sensor: the acquisition of strain in the presence of important temperature excursions require the use of two FBG sensors in pairs, one for the strain, which is bonded to the structure of interest, and one for the temperature, close to the first but isolated from strain, responding to temperature variations only.

FBG sensors allow distributed sensing over significant areas by multiplexing a large number of sensors on a single fibre, are immune to electromagnetic interference and have compact size. For all these advantages, they have been widely used in many applications for the structural health monitoring [22, 26].

The core of the system is the embedding of one, or more, optical fiber equipped with several FBG sensors along the tire circumference. In the present work, one FBG sensor is pasted on the internal surface of the tire [3], as in Fig. 1.

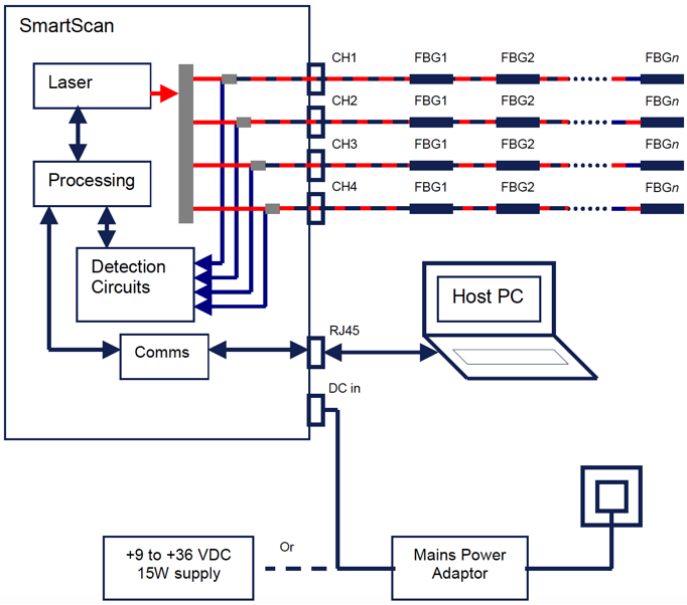

Figure 2: Measurement scheme of the OPTYRE system.

The measurement scheme is shown in Fig. 2, whose schematic description is provided ahead:

- A light beam signal, in the range of far infrared wavelengths, is generated by an optical led source; the light beam travels along an optical fiber equipped with FBG sensors attached to the tire circumference.
- When the tire is deformed, the frequency bandwidth of the reflected light changes and such variation is detected by a spectrum analyser.
- The spectrum analyser samples the analogical signal before sending it to the computer, where the signal can be suitably processed.

The interrogator reads the instantaneous wavelength of each FBG sensor, which is related to the local strain ε by the formula:

$$\varepsilon_j(t) = K_\varepsilon \frac{\lambda_j(t) - \lambda_{0j}}{\lambda_{0j}} - \alpha \Delta T \quad (1)$$

Where λ_{0j} is the reference wavelength for the j-th FBG sensor, $K_\varepsilon = 1.27$ is the constant of proportionality, ΔT is the temperature variation during the experiment, which is roughly zero in our tests, and α is the coefficient of thermal expansion.

The FBG interrogator is integral with the car chassis therefore, to allow the acquisition under dynamic condition, a fiber optic rotary coupler, in Fig. 3, is interposed between the tire and the interrogator. The rotary joints are to optical signals what electrical slip rings are to electrical signals, or the transmitter for radio waves devices, a means to pass signals across rotating interfaces, allowing uninterrupted data transmission while rotating. The rotoric flange of the coupler has to be coaxial with the tire axes and integral with the rim, while the statoric flange has to be rigidly connected with the car chassis. These tasks are carried out with a properly designed coupler case, in Fig. 4, which protects the rotary joint from rubbles and allows an easy connection to the wheel.

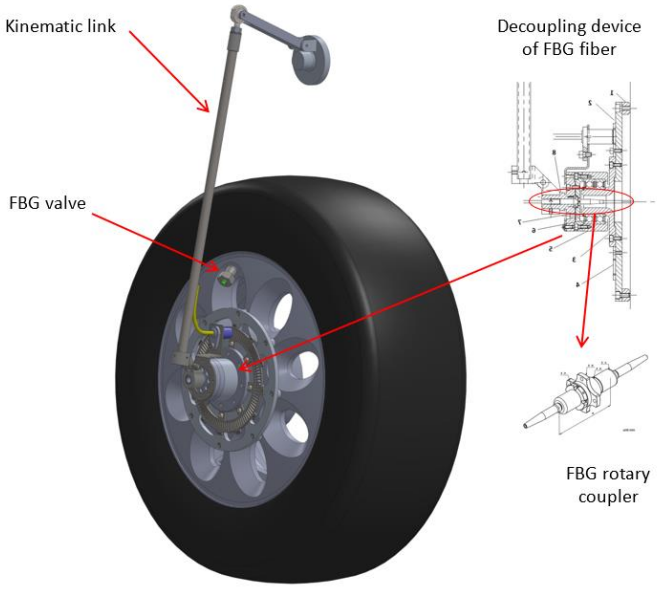

Figure 3: CAD of the wheel with in evidence the FBG rotary coupler and the kinematic link.

The present setup overcomes the main difficulties of the technologies of the prior art, both related to the power supply system and to the data transmission system. The power generator supplying the FBG sensors is integral to the affixed parts of the vehicle and external to the tire; this generator consists of one light source that transmits light to the fibre optic, which is integral to the tire carcass, by means of the contactless rotary optical coupler. The optical signal sent on-board the tire is modulated passing through the FBG sensors and reflected outside the tire by means of the rotary optical coupler itself, which thus replaces each data transmission device. One of the main advantage of this technological solution is that the same physical light beam carries both the power to sensors and the information to the interrogator. Further advantages of the present setup arise from the material of these sensors, which have low rigidity and are capable of long-term acquisitions, even under adverse conditions encountered by the tires, and are highly compatible with the rubber of the tire. The tire used for the present setup has the size 215/45 R17, it is installed on a prototype vehicle shown in Fig. 4.

Figure 4: Support case onboard installation.

3 Rolling resistance model of a rolling tire

3.1 Analytical model for the strain distribution over the tire surface

The tire optimal design is a trade-off of conflicting goals [21], such as tire weight, directional stability, wet handling, ride comfort, steering feel, service life and rolling resistance. Given the complexity on the optimal design of the tire both theoretical models and experiments are needed.

A propaedeutic analysis based on a simple theory of strain along a rotating tire is needed before showing the experimental results. In fact, this theoretical background helps in an easier interpretation of the experiments and allows for closed form solutions. The focus is therefore to develop a model for the understanding of the strain trend along the entire circumferences of the tire, which is used to predict the rolling resistance within the tire.

A simple theory of strain along a rotating tire was proposed in [3], the model allows a closed form solution, enabling the identification of the position of the transition between slip and non-slip regions and of the length and position of the tire-road contact patch. Following a similar approach, it is here studied how the presence of viscous damping affects the deformation of a rotating tire.

The toroidal shape of the tire is rectified, the tread is assumed to have the characteristics of an infinite beam attached to the elastic structure of the sidewalls, which is modelled with an elastic foundation of the Winkler type. Thus, the transverse vibration w of the beam is described by the differential equation:

$$EJ\frac{\partial^4 w(x,t)}{\partial x^4} + \mu\frac{\partial^2 w(x,t)}{\partial t^2} + 2\mu\omega_d\frac{\partial w(x,t)}{\partial t} + kw(x,t) = P\delta(x-ct) \tag{2}$$

where x and t are the space and time independent variables and EJ, μ, ω_d, k are the flexural stiffness, the mass per unit length, the circular frequency of damping and the coefficient of Winkler foundation, respectively. P is the vertical load that, for the sake of simplicity, it is assumed punctual and constant, which moves with a constant velocity c and $\delta(x)$ is the Dirac delta function.

The quasi-stationary solution is obtained introducing the independent variable $s = \lambda(x - ct)$, with $\lambda = \sqrt[4]{\frac{k}{4EJ}}$, the solution of the eq. (2) will be in the form $w(x,t) = w_0\tilde{w}(s)$, which is the product between the

dimensionless deflection and the static deflection of beam: $w_0 = \frac{P}{8\lambda^3 EJ} = \frac{P\lambda}{2k}$. Substituting the previous terms into eq. (2), after some algebra, gives the ordinary differential equation of the fourth order:

$$\frac{d^4\widetilde{w}(s)}{ds^4} + 4\alpha^2 \frac{d^2\widetilde{w}(s)}{ds^2} - 8\alpha\beta \frac{d\widetilde{w}(s)}{ds} + 4\widetilde{w}(s) = 8\delta(s) \tag{3}$$

where the dimensionless parameters are:

$$\alpha = \frac{c}{c_{cr}} = \frac{c}{2\lambda}\sqrt{\frac{EJ}{\mu}}, \quad \beta = \sqrt{\frac{\mu}{k}}\omega_d \tag{4}$$

with:

$$c_{cr} = 2\lambda\sqrt{\frac{EJ}{\mu}} \tag{5}$$

the critical speed of the beam.

Using the following boundary conditions:

$$s \to \pm\infty: \qquad \widetilde{w}(s) = \widetilde{w}'(s) = \widetilde{w}''(s) = \widetilde{w}'''(s) = 0 \tag{6}$$

The solution of eq. (6) is found by the method of Fourier integral transformations:

$$\begin{aligned} \widetilde{w}(s) &= \frac{2}{a_1\left(D_1^2 + D_2^2\right)} e^{-bs}(D_1 \ \cos a_1 s + D_2 \ \sin a_1 s), \quad \text{with } s \geq 0 \\ \widetilde{w}(s) &= \frac{2}{a_2\left(D_3^2 + D_4^2\right)} e^{bs}(D_3 \ \cos a_2 s - D_4 \ \sin a_2 s), \quad \text{with } s < 0 \end{aligned} \tag{7}$$

with:

$$\begin{aligned} D_{1,3} &= a_{1,2} b \\ D_{2,4} &= b^2 \mp \frac{1}{4}(a_1^2 - a_2^2) \end{aligned} \tag{8}$$

and the following constants are obtained for light damping, i.e. β<<1:

$$b = \sqrt{1 - \alpha^2}, \quad a_{1,2} = \sqrt{1 + \alpha^2 \pm \frac{2\alpha\beta}{b}} \tag{9}$$

In absence of dissipation $a_1 \equiv a_2 = a = \sqrt{1 + \alpha^2}$ and the undamped expression for eq. (7) is:

$$\widetilde{w}_{ud}(s) = \frac{e^{-b|s|}}{ab}(a \cos as + b \sin a|s|) \tag{10}$$

that is an even function of the variable *s*. In order to understand how dissipation modifies the system response, the Taylor expansion of the function $\widetilde{w}$ in terms of the parameter β up to the order 2 is performed, after some algebra, it holds:

$$\widetilde{w}(s) \approx \widetilde{w}_{ud}(s) - \text{sign}(s)\frac{\alpha\beta}{ab}\left[\frac{1}{a}\widetilde{w}_{ud}(s) + \frac{1}{b}\frac{e^{-b|s|}}{ab}(1 + b|s|)(b \cos as - a \sin a|s|)\right] \tag{11}$$

The terms within the square brackets on the left hand side are even functions, which are multiplied by an odd function and give rise to an odd function:

$$\psi(s) = -\text{sign}(s)\left[\frac{1}{a}\widetilde{w}_{ud}(s) + \frac{1+b|s|}{b}\frac{e^{-b|s|}}{ab}(b \cos as - a \sin a|s|)\right] \tag{12}$$

Introducing the small parameter $\epsilon = \frac{\alpha\beta}{ab} \ll 1$, which linearly depends on the amount of damping β, the damped deformation $\widetilde{w}(s)$ can be regarded as the undamped response slightly perturbed by an odd function:

$$\widetilde{w}(s) \approx \widetilde{w}_{ud}(s) + \epsilon\psi(s) \tag{13}$$

Through the stress-strain relationship, the beam deformation is given by:

$$\varepsilon = -\frac{M}{EJ}y = -w''y \tag{14}$$

where ε is the strain in the *x* direction at distance *y* from the neutral axis. In the same fashion, also the circumferential strain can be regarded as an even function slightly perturbed by an odd one:

$$\varepsilon(s) \approx \varepsilon_{ud}(s) + \epsilon\varphi(s) \tag{15}$$

To provide the evidence of eq. (13), the functions $\widetilde{w}(s)$ and $\widetilde{w}_{ud}(s)$, evaluated with eq.s (7) and (10), respectively, and their difference $\widetilde{\Delta w}(s) = \widetilde{w}(s) - \widetilde{w}_{ud}(s)$, are plotted in Fig. 5 using the parameters listed in Tab. 1. The Fig. 5 shows $\widetilde{\Delta w}(s)$ is actually an odd function, whose amplitude is small.

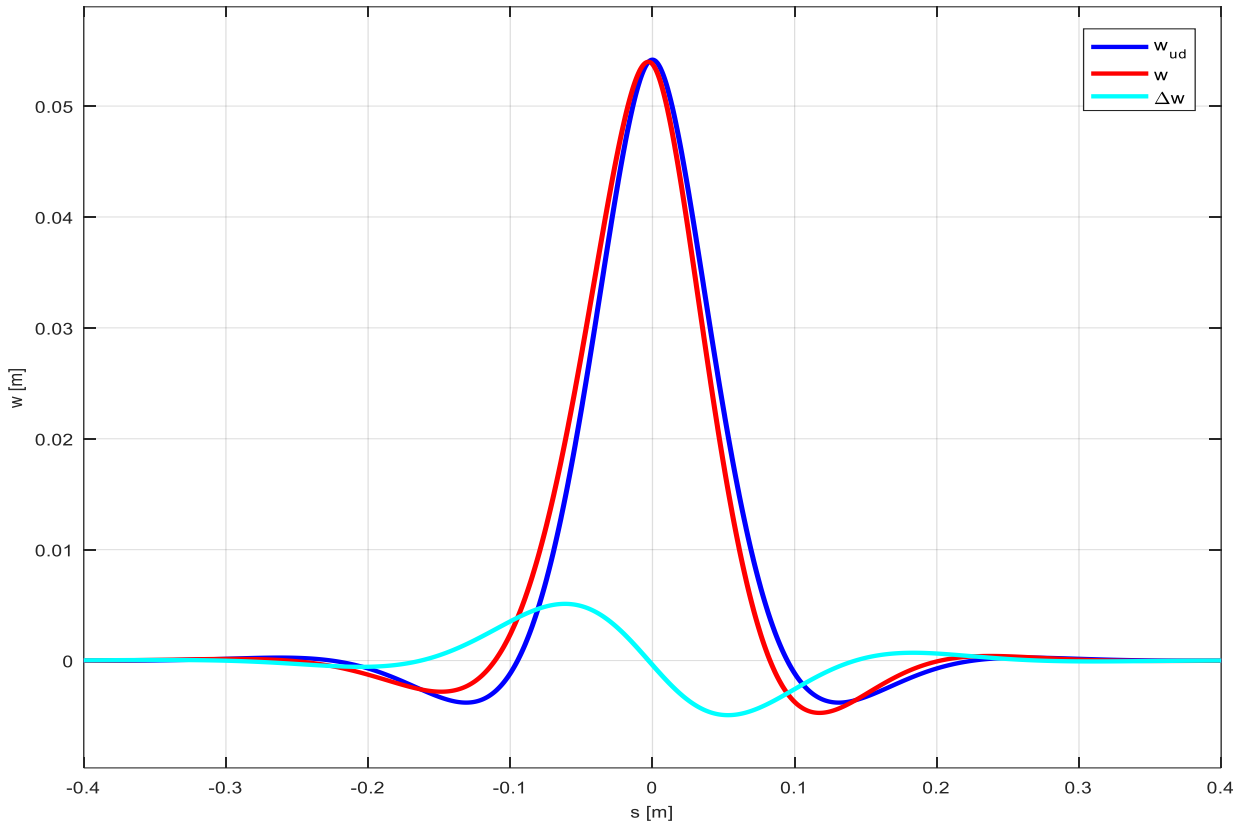

Figure 5: Undamped, damped vertical deflections and their difference in function of the variable *s*.

List of symbols	
E=5·10^7 N	Tire Young modulus
J=1.66·10^{-8} m^4	Beam area moment of inertia
μ=1100 kg/m	Tire mass per unit length
k=7.790·10^6 N/m^2	Elastic constant of the Winkler foundation
R=0.3126 m	Unloaded radius of the tire
h_t=0.018 m	Tire section height
L=0.05 m	Semi footprint length
M=400·9.81 N	Total load over the footprint
C_x=1.883·10^6 N/m	Longitudinal slip coefficient
f_s=0.8	Static tire-road friction coefficient
f_d=0.6	Kinematic tire-road friction coefficient
c= 11.11 m/s	Speed of the moving load

Table 1: List of symbols and their values.

3.2 Analytical model for the rolling resistance

As shown in the previous section, the normal pressure in the leading half of the footprint is higher than that in the trailing half, thus the vertical resultant force is offset towards the front of the footprint and generates a torque on the wheel that contrasts its forward motion. This phenomenon is mainly caused by the hysteresis in the tire due to the deflection of the carcass while rolling and gives rise to rolling resistance. The energy dissipation induced by deformation is the cause of roughly 90% of rolling resistance [2], and it is therefore related to the materials of which tires are made. The tire operating conditions affect rolling resistance, such as load, inflation pressure, temperature and, in a lower measure, the car travelling speed.

The main object of the present section is to provide an estimation of the energy loss due to rolling resistance that relies on easily measurable parameters, such as the circumferential strain or geometric characteristics of the tire.

Using a rather general approach, it is derived a relationship between the rate of external work, the rate of internal working and the kinetic energy within a deformable solid. To this aim, let $P(V,t)$ the rate at which external work is being done on any part V of the body bounded by the surface A in the deformed solid at the instant t. It holds:

$$P(V,t) = \int_V \rho \mathbf{b} \cdot \mathbf{v} \mathrm{d}V + \int_A \mathbf{T} \cdot \mathbf{v} \mathrm{d}A \tag{16}$$

where ρ is the mass density function in the current configuration, **b** is the body force per unit mass distributed over the volume V, **T** is the contact force per unit area or traction, **v** is the particle velocity at the point **x**. The variables in eq. (16) are configuration and time dependent, for the sake of notation the explicit dependence to (**x**,t) was not displayed and will be omitted in the following equations.

Considering infinitesimal motions the traction **T** becomes the projection of the Cauchy stress tensor **σ** along the outward normal unit vector **n** to the surface A, i.e. $T_i=\sigma_{ij}n_j$ where the Einstein summation convention has been adopted, using the divergence theorem and writing out in full eq. (16) becomes:

$$P(V,t) = \int_V \left(\rho b_i v_i + \frac{\partial \sigma_{ij} v_i}{\partial x_j}\right) \mathrm{d}V \tag{17}$$

Considering the linear momentum balance in terms of Cauchy stress:

$$\rho \frac{\partial v_i}{\partial t} = \frac{\partial \sigma_{ij}}{\partial x_j} + \frac{\partial \sigma_{ij}}{\partial x_j} + \rho b_i \tag{18}$$

substituting eq. (18) into eq. (17) and using the symmetry of the stress tensor holds:

$$P(V,t) = \int_V \left[\frac{1}{2}\rho \frac{\partial (v_i v_i)}{\partial t} + \frac{1}{2}\sigma_{ij}\left(\frac{\partial v_i}{\partial x_j} + \frac{\partial v_j}{\partial x_i}\right)\right] \mathrm{d}V \tag{19}$$

Finally, let $\dot{\varepsilon}_{ij} = \frac{\partial \varepsilon_{ij}}{\partial t} = \frac{1}{2}\left(\frac{\partial v_i}{\partial x_j} + \frac{\partial v_j}{\partial x_i}\right)$ the strain rate tensor and combing eq. (19) and eq. (16), the work-energy relation is found:

$$\int_V \rho b_i v_i \mathrm{d}V + \int_A T_i v_i \mathrm{d}A = \int_V \left(\frac{1}{2}\rho \frac{\partial (v_i v_i)}{\partial t} + \sigma_{ij}\dot{\varepsilon}_{ij}\right) \mathrm{d}V \tag{20}$$

Eq. (20) states that the rate of external work on any part of the body equals the rate of increase of kinetic energy and the rate of internal work within that part, which is the last term of the right hand side and is often called the stress power. Generally, the stress power accounts for both stored and dissipated energy.

The aim is now to express the power dissipated by the tire in terms of the acquired circumferential strain. Following a similar approach than the one outlined in section 2, the tread is assumed to behave like an isotropic viscoelastic beam (Newtonian fluid dissipation model) that undergoes longitudinal and flexural vibrations along x- and z-directions, as depicted in Fig. 6. Under these hypotheses, the strain tensor becomes:

$$\begin{aligned} \varepsilon_{11} &= \frac{\partial u(x_1,t)}{\partial x_1} + x_3 \frac{\partial \theta(x_1,t)}{\partial x_1} \\ \varepsilon_{13} = \varepsilon_{31} &= \frac{\partial w(x_1,t)}{\partial x_1} + \theta(x_1,t) \end{aligned} \tag{21}$$

where indexes 1 and 3 are for x and z axis, thus x_1=x and x_3=z, u and w are the longitudinal and vertical displacements and θ is the rotation of the cross section of the beam around y axis, as depicted in Fig. 6. Considering the first line in eq. (21) the first and second term on the right hand side are the longitudinal and flexural contribution, respectively, to the beam deformation along the x axis, while the second line in eq. (21) is due to the shear deformation induced by the flexural displacement only. The viscoelastic constitutive equation leads to:

$$\begin{aligned} \sigma_{11} &= E\varepsilon_{11} + \eta\dot{\varepsilon}_{11} \\ \sigma_{13} &= \sigma_{31} = G\varepsilon_{13} + \eta\dot{\varepsilon}_{13} \end{aligned} \tag{22}$$

where E and G are the Young and shear modulus, respectively, and η is the viscous damping coefficient.

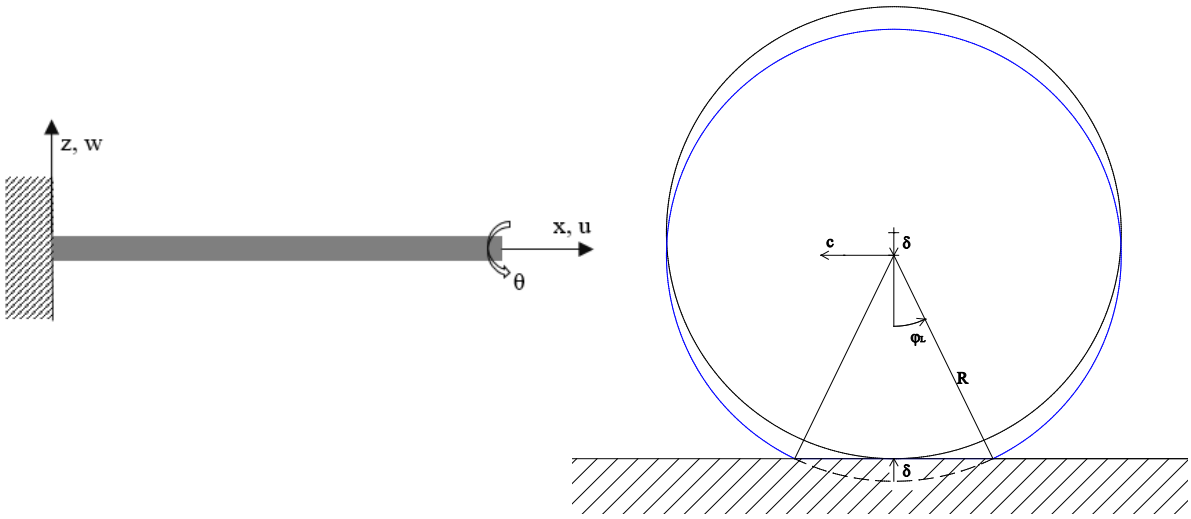

Figure 6: Reference systems for the elastic beam and the rolling tire.

While longitudinal deformations can be measured with the embedded system described in section 2, vertical displacements and, especially, cross section rotations are challenging to measure and are not experimentally acquired in the present work. In order to provide a qualitative yet significant formulation, the following assumptions are made:

i. Euler-Bernoulli beam is considered, it implies $\theta(x,t) = -\frac{\partial w}{\partial x}$, thus the shear deformation and strain terms in eq. (21) and (22) are equal to zero and $\varepsilon_{11} = \frac{\partial u}{\partial x} - z\frac{\partial^2 w}{\partial^2 x}$.

ii. Replacing the curvilinear abscissa Rφ with the independent variable x and considering a stationary motion, the new independent variable s is introduced: $s = R(\varphi + \omega t)$. The origin moves together with the rolling tire with angular speed ω, the sign + on the right hand side arises from the sign conventions in Fig. 6 and indicates that, for positive rotations, the velocity of the centre of the tire has opposite direction than the x-axis.

Under these assumptions, the partial derivatives become $\frac{\partial}{\partial x} = \frac{d}{ds}$ and $\frac{\partial}{\partial t} = R\omega\frac{d}{ds}$, the longitudinal deformation in eq. (21) is now expressed in terms of the measured strain acquired within the inner surface of the tire at $z = \frac{h}{2}$, i.e. $\varepsilon_m = \varepsilon_{11}\left(s, \frac{h}{2}\right)$, as follows:

$$\begin{aligned} u' &= \varepsilon_m + \frac{h}{2}w''; \;\; u'' = \varepsilon_m' + \frac{h}{2}w''' \\ \varepsilon_{11} &= \varepsilon_m + \left(\frac{h}{2} - z\right)w''; \; \frac{\partial\varepsilon_{11}}{\partial t} = R\omega\left(\varepsilon_m' + \left(\frac{h}{2} - z\right)w'''\right) \end{aligned} \tag{23}$$

where $(\;\;)' = \frac{d}{ds}(\;\;)$ and, for the sake of notation, the dependence (s) has been omitted. Using eq. (23) into the first term on the right hand side in eq. (20), the kinetic term becomes:

$$K(\varepsilon_m, \varepsilon_m', \mathrm{w}', \mathrm{w}'', \mathrm{w}''') = \int_V \frac{1}{2}\rho \frac{\partial(\mathrm{v}_i \mathrm{v}_i)}{\partial t} \mathrm{dV} = \mathrm{A}(\mathrm{R}\omega)^3 \rho \int_{-\pi R}^{\pi R} (\mathrm{u}'\mathrm{u}'' + \mathrm{w}'\mathrm{w}'') \mathrm{ds} = \\ = \mathrm{A}(\mathrm{R}\omega)^3 \rho \int_{-\pi R}^{\pi R} \left(\varepsilon_m \varepsilon_m' + \frac{h}{2}(\varepsilon_m \mathrm{w}''' + \varepsilon_m' \mathrm{w}'') + \frac{h^2}{4} \mathrm{w}'' \mathrm{w}''' + \mathrm{w}' \mathrm{w}'' \right) \mathrm{ds} \tag{24}$$

where A is the cross section of the beam. Similarly, the second term on the right hand side in eq. (20), which is the stress power, becomes:

$$S(\varepsilon_m, \varepsilon_m', \mathrm{w}'', \mathrm{w}''') = \int_V \sigma_{ij} \dot{\varepsilon}_{ij} \mathrm{dV} = \mathrm{R}\omega \mathrm{E} \int_V \varepsilon_{11} \varepsilon_{11}' \mathrm{dV} + (\mathrm{R}\omega)^2 \eta \int_V {\varepsilon_{11}'}^2 \mathrm{dV} = \\ \mathrm{R}\omega \mathrm{EA} \int_{-\pi R}^{\pi R} \left(\varepsilon_m \varepsilon_m' + \frac{h}{2}(\varepsilon_m \mathrm{w}''' + \varepsilon_m' \mathrm{w}'') + \frac{h^2}{3} \mathrm{w}'' \mathrm{w}''' \right) \mathrm{ds} \\ + (\mathrm{R}\omega)^2 \eta \mathrm{A} \int_{-\pi R}^{\pi R} \left({\varepsilon_m'}^2 + h \varepsilon_m' \mathrm{w}''' + \frac{h^2}{3} {\mathrm{w}'''}^2 \right) \mathrm{ds} \tag{25}$$

Eq. (24) and (25) provide the internal rate of energy in terms of the measured strain and in terms of the vertical displacement and its derivatives. Accordingly with the theoretical findings of the previous section, for light dissipation the vertical displacements and the circumferential deformation can be approximated by even functions that are slightly perturbed by odd ones, thus, for example, the first term on the right hand side in eq. (24) becomes:

$$\int_{-\pi R}^{\pi R} \varepsilon_m \varepsilon_m' \mathrm{ds} \approx \int_{-\pi R}^{\pi R} \left(\varepsilon_{ud} \varepsilon_{ud}' + \epsilon \varepsilon_{ud} \varphi' + \epsilon \varepsilon_{ud}' \varphi \quad + \epsilon^2 \varphi \varphi' \right) \mathrm{ds} \tag{26}$$

In eq. (26) odd integrands provide null contributions while even integrands are multiplied by the small parameter ϵ, thus their integrals are very small. Therefore, the rate of increase of kinetic energy K and the elastic terms within the stress power S provide a very small contribution, for each tire revolution, to the internal power dissipation, which goes to zero for vanishing damping coefficients. Thus, the only term that is retained on the right hand side of eq. (20) is:

$$K + S \approx (\mathrm{R}\omega)^2 \eta \mathrm{A} \int_{-\pi R}^{\pi R} {\varepsilon_m'}^2 \mathrm{ds} \tag{27}$$

The internal dissipated power depends explicitly on the square linear velocity of the tire, it can be easily computed by numerical integration once the circumferential strain has been measured by the embedded FBG sensors, as it is shown in the next section.

A final mention deserves the future perspectives of the tire modelling in the context of embedded sensor-based real-time identification techniques. In fact, in this paper it has been emphasized how, for real-time sensing, semi-analytical models are particularly appealing. Under this point of view, the developed analytical model represents a good compromise between a reasonable realistic description of the strain-grip correlation and the need of a sufficiently fast algorithm for real-time use. However, the experience of the Optyre Project has suggested further direction of investigation, trying to include into a relatively simple model also the following aspects: (i) impact dynamics at the leading edge, in a way similar to that presented in [23, 27], (ii) a richer phenomenology in contact mechanics between rough surfaces, making use of the theory in [12], (iii) implementation of new higher-order stress-strain constitutive relationship to account in a synthetic manner of the complex composite structure of the tire, through models close to those in [7, 28], (iv) modelling the contact mechanics in the presence of an interstitial fluid (tire-water-road contact), following some of the ideas contained in [8].

4 Field Experiments and Discussion

This section displays the results of the experimental campaign under dynamic conditions, driving the car on country roads. The tests was carried out with three passengers on board, the measured static weight on the rear left tire (where FBG sensors are placed) was of 350 kg, the tire pressure was 2.2 atm.

Fig. 7 shows a typical circumferential strain signal, acquired along the inner surface of the tire, with the car undergoing a standing start, accelerations, uniform speed drives and braking manoeuvres. Fig. 8 shows a magnification of the plot in Fig. 7 taken during uniform speed derive: results are in line with the findings of section 2, the sensor is placed on the inner surface of the tire, thus the area within the contact patch is mainly stretched.

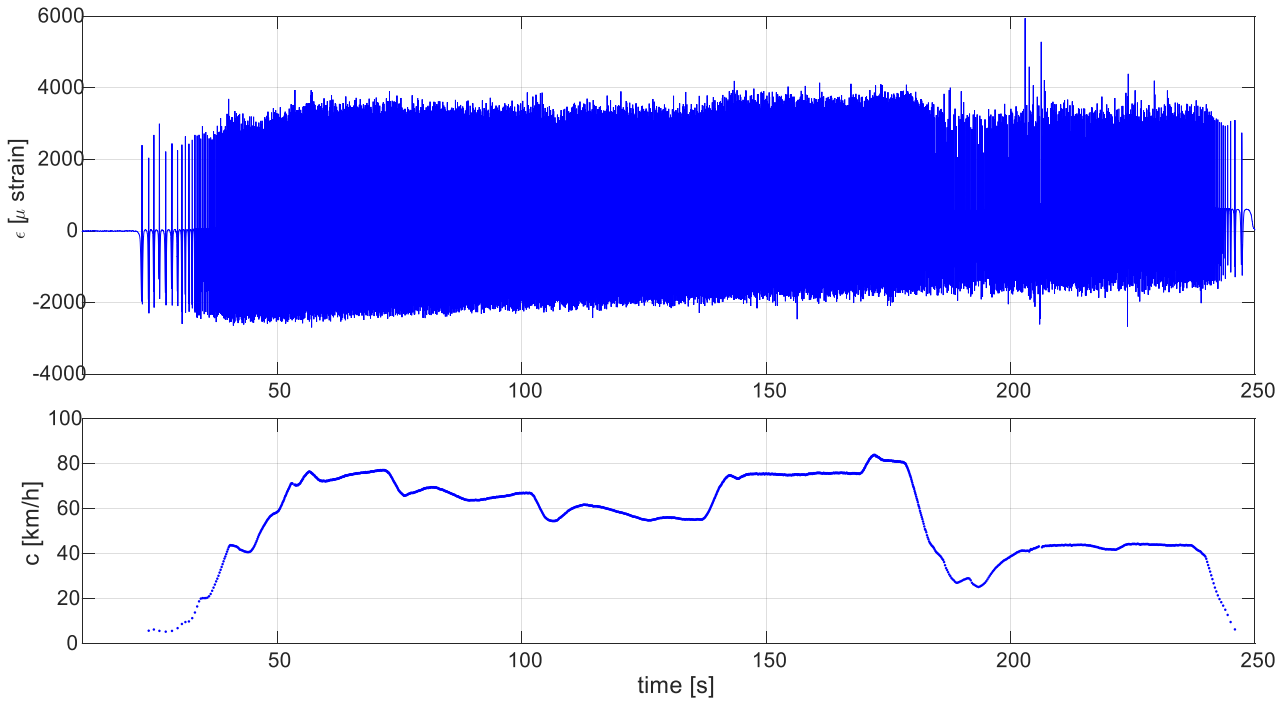

Figure 7: Starting from the subplot on top, the dynamic strain and the estimated tire velocity plotted versus time, red line is for the smoothed signal.

The tire velocity is estimated from the strain signal, considering that the maximum strain points are roughly in correspondence of the centre of the footprint. Given the spatial distance between two consecutive peaks, of about $2\pi R$, the tire speed is numerically estimated with a 2nd order centred differencing formula, with the aid of a peak identification algorithm, i.e. findpeaks function in Matlab™, applied to the strain time history in Fig. 7. The second subplot shows the estimated velocity.

At the begin of the acquisition the tire is cold then tire's cyclical distortion generates hysteresis loss, which is converted to heat and makes the temperature of the tire rising, as it appears from the slow drift of the average strain in Fig. 7. In fact, given the linear relationship between temperature and tire inflation pressure, at early times the strain is roughly zero when the FBG sensors is in correspondence of the unloaded position, i.e. diametrically opposed to the contact patch centre, while at the end of the acquisition the circumferential deformation is roughly 600 μstrain.

Using the definition of dissipated power given in eq. (27), the specific power P_d, is introduced:

$$P_d = (\mathrm{R}\omega)^2 \mathrm{A} \int_{-\pi R}^{\pi R} {\varepsilon'_m}^2 \mathrm{ds} \tag{28}$$

Eq. (28) is plotted in Fig. 9: fluctuations are mostly caused by road irregularities since the tire velocity is almost constant on the selected time interval.

Fig. 10 shows the time history of P_d over the whole acquisition interval. In order to smooth the data, the moving average is evaluated within those time intervals where the tire velocity remains almost constant, i.e. where the constraint $c(t_i) - c(t_{i-1}) < 0.08\ m/s$ is satisfied. To better understand the relation between the dissipated power and the tire velocity the dissipation factor p_d is introduced:

$$p_d = \frac{P_d}{(\mathrm{R}\omega)^2 \mathrm{A}} = \int_{-\pi R}^{\pi R} {\varepsilon'_m}^2 \mathrm{ds} \tag{29}$$

that is plotted in the second subplot of Fig. 10. The smoothed values of Fig. 10 are sorted in ascending order in respect of the tire velocity and plotted in Fig. 11. The dissipation factor decreases almost linearly as the tire speed increases, as a result, the specific power values are well approximated by an increasing linear fit.

The dispersion of the values around the regression lines are due to inertia forces arising from transient manoeuvres, i.e. heavy breaking or accelerating, and from road irregularities.

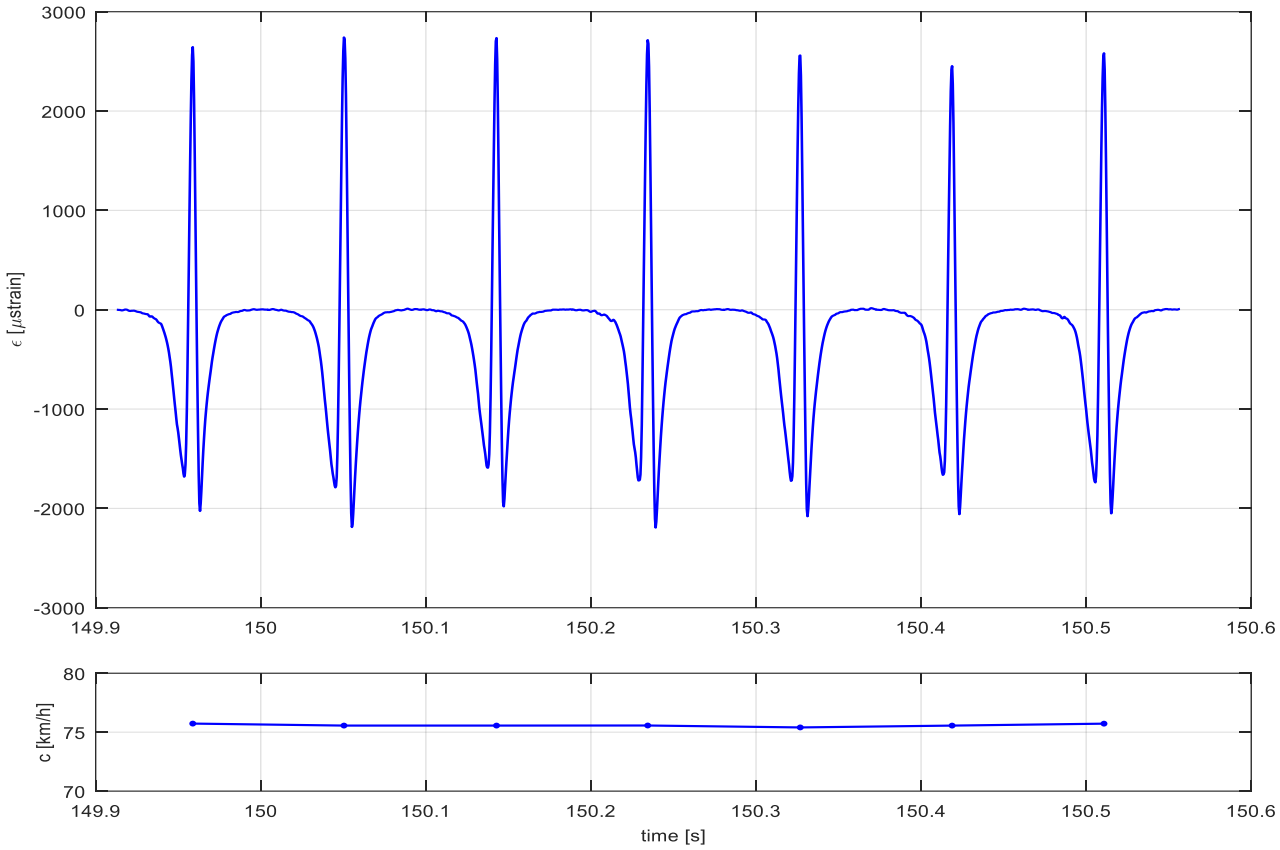

Figure 8: Magnification of the strain plot in Fig. 7 between 150 and 150.5 s.

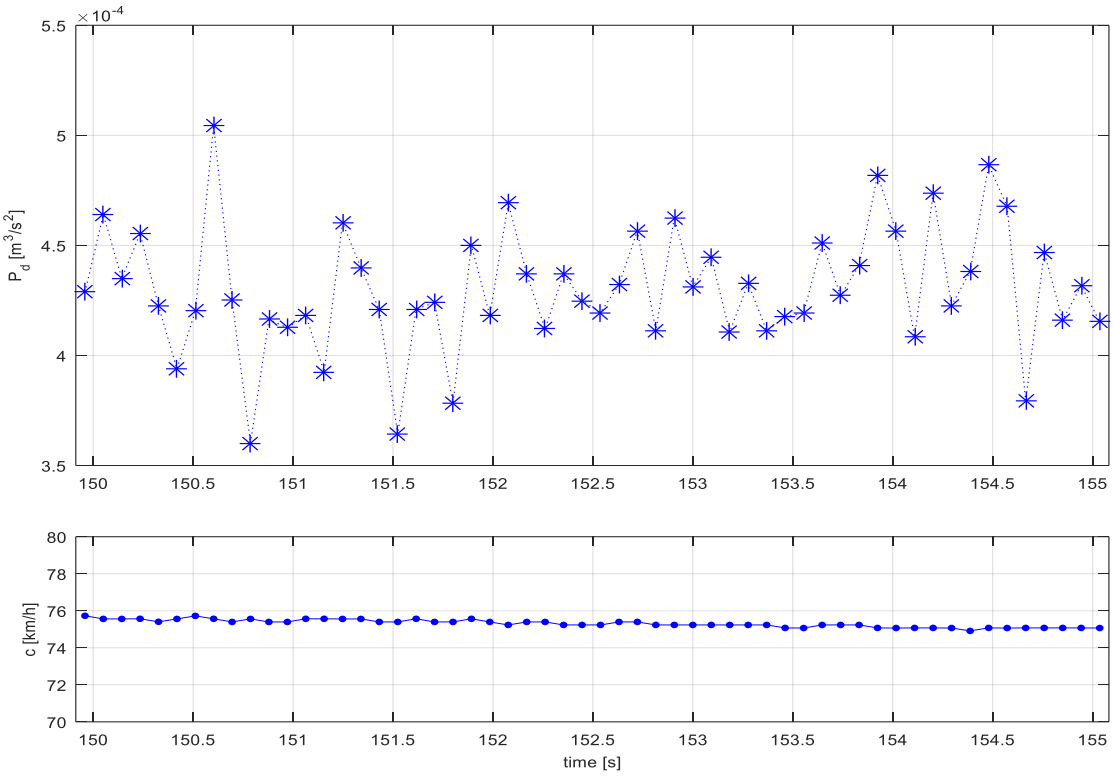

Figure 9: Specific dissipated power between 150 and 155 s.

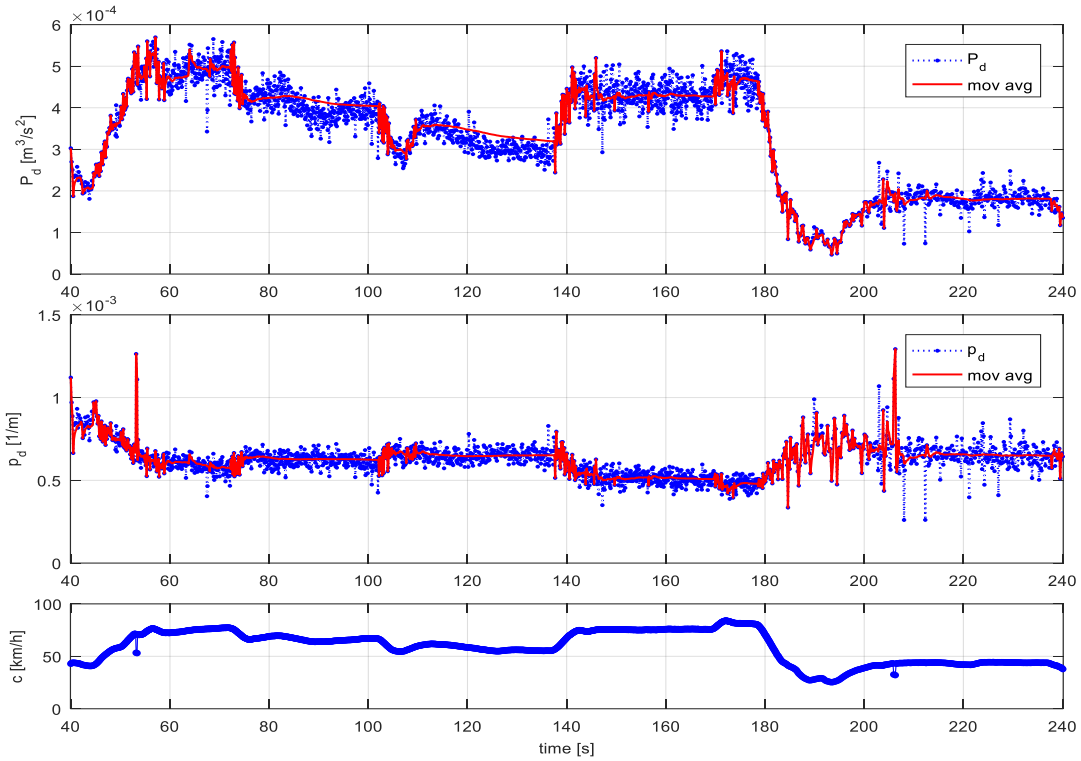

Figure 10: In the first subplot the specific dissipated power and its moving average in blue and red lines, respectively, in the second subplot the dissipation factor and its moving average, in the third subplot the estimated velocity of the centre of the tire, plotted versus time.

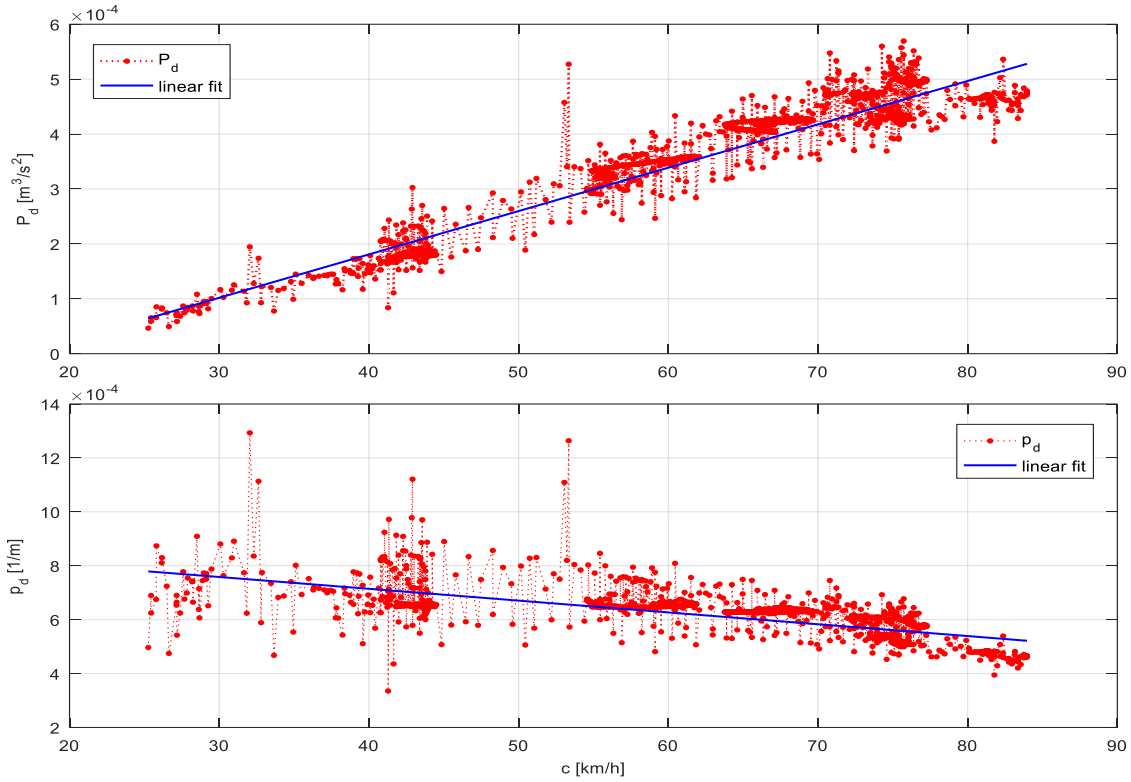

Figure 11: In the first and second subplot the moving averages of the specific dissipated power and of the dissipation factor, evaluated in Fig. 10, sorted in ascending order in respect of the tire velocity, along the *x*-axis.

5 Concluding remarks

The proposed algorithm together with the experimental apparatus, developed within the OPTYRE project and briefly presented in this paper, set the basis for a new system for the real-time identification of the tire stress during rolling and the residual grip estimation.

The optical experimental setup allows the measurement of strain signals with high resolution and accuracy, it does not need complex power supply or data transmission systems, and it is capable of long-term acquisitions, under adverse conditions.

A new analytical model of the tire is presented, which permits to express the dissipated power in terms of the circumferential strain, and provides a qualitative yet significant description of the tire-road interaction. The internal dissipated power also depends explicitly on the square linear velocity of the tire, and it can be easily computed, cycle after cycle, once the circumferential strain is being measured by the embedded FBG sensors.

For real-time sensing, semi-analytical models are particularly appealing, since they permit a higher speed in the real-time data analysis and in the identification process. Under this point of view, the developed analytical model represents a good compromise between a reasonable realistic description of the strain-grip correlation and the need of a sufficiently fast algorithm for real-time use. Theoretical and experimental results open the way for the real time identification of the tire rolling resistance and, more generally, of the tire-road grip conditions. At the moment, a phonic wheel is mounted on the rim and another experimental campaign is being carried out to get further insights into these open topics.

References

[1] Epa, Climate Change Indicators in the United States, 2014 Third Edition, available online.

[2] Michelin, *The tire: rolling resistance and fuel savings*, 2003, available online.

[3] N. Roveri, G. Pepe, A. Carcaterra, *OPTYRE – A new technology for tire monitoring: Evidence of contact patch phenomena*, Mechanical Systems and Signal Processing, 66-67, (2016) 793–810.

[4] S.C. Ergen, A. Sangiovanni-Vincentelli, X. Sun, R. Tebano, S. Alalusi, G. Audisio, M. Sabatini, *The Tire as an Intelligent Sensor*, *Computer-Aided Design of Integrated Circuits and Systems*, IEEE Transactions, 28, no.7 (2009), 941 – 955.

[5] H. Morinaga, Y. Wakao, Y. Hanatsuka, A. Kobayashi, *The possibility of intelligent tire*, *Proceedings of 31st FISITA Automotive*, Congress Yokohama, Japan, 2006. p.F2006V104.

[6] A. Carcaterra, N. Roveri, *Tire grip identification based on strain information: Theory and simulations*, Mechanical Systems and Signal Processing, 41(1–2), 2013, 564–580.

[7] F. dell'Isola, P. Seppecher, *The relationship between edge contact forces, double forces and interstitial working allowed by the principle of virtual power*, Comptes Rendus de l'Academie de Sciences – Series IIb: Mecanique, Physique, Chimie, Astronomie, 321 (1995), 303-308.

[8] F. dell'Isola, A. Madeo, P. Seppecher, *Boundary conditions at fluid-permeable interfaces in porous media: A variational approach*, International Journal of Solids and Structures, 46, no. 17 (2009), 3150-3164.

[9] A. Carcaterra, N. Roveri, M. Platini, *Device and method for optically measuring the grip of a tire and tire suitable for said measuring property*, University of Rome "La Sapienza", first deposit number RM2011A000401, date 27/07/2011.

[10] G. Audisio, *The Birth of the Cyber Tyre*, Solid-State Circuits Magazine, IEEE Transactions, 2, no.4 (2010), 16 – 21.

[11] N. Roveri, A. Carcaterra, A. Akay, *Frequency intermittency and energy pumping by linear attachments*, Journal of Sound and Vibration, Available online 14 May 2014, http://dx.doi.org/10.1016/j.jsv.2014.04.003.

[12] A. Misra, S. Huang, *Micromechanics based stress-displacement relationships of rough contacts: Numerical implementation under combined normal and shear loading*, Computer Modeling in Engineering and Sciences, 52, no. 2 (2009), 197-215.

[13] B. Glisic, D. Inaudi, *Fibre Optic Methods for Structural Health Monitoring*, New York: Wiley, 2007.

[14] A. Carcaterra, N. Roveri, G. Pepe, *Fractional dissipation generated by hidden wave-fields*, Mathematics and Mechanics of Solids 1081286513518941, first published on January 13, 2014 as doi:10.1177/1081286513518941.

[15] L. Chankyu, Mechatronics, IEEE/ASME Transactions on 9, 454 (2004).

[16] J. Yi, Control Systems Technology, IEEE Transactions on 10, 381 (2002).

[17] Z. Xiangwen, in Intelligent Vehicles Symposium, 2005. Proceedings. IEEE. (2005), pp. 875-881.

[18] F. Gustafsson, SAE Tech. Papers 2001-01-0796, (2001).

[19] M. Nabipoor, Journal of Physics: Conference Series 34, 770 (2006).

[20] A. Pohl, Instrumentation and Measurement, IEEE Transactions on 48, 1041 (1999).

[21] G. Genta, The Automotive Chassis, Springer, 2009.

[22] N. Roveri, A.Carcaterra, A.Sestieri, *Real-time monitoring of railway infrastructures using fibre Bragg grating sensors*, Mechanical Systems and Signal Processing, 60-61, (2015), 14–28.

[23] U. Andreaus, L. Placidi, G. Rega, *Soft impact dynamics of a cantilever beam: equivalent SDOF model versus infinite-dimensional system*, *Proceedings of the Institution of Mechanical Engineers*, Part C: Journal of Mechanical Engineering Science, 225, no. 10 (2011), 2444-2456.

[24] N. Roveri, A. Carcaterra, *Unsupervised identification of damage and load characteristics in time-varying systems*, Continuum Mechanics and Thermodynamics, 2013, DOI 10.1007/s00161-013-0328-3.

[25] C.R. Carlson, J.C. Gerdes. *Consistent nonlinear estimation of longitudinal tire stiffness and effective radius*, IEEE Transactions on Control Systems Technology, 13(6):1010–1020, 2005.

[26] A. Sestieri, *New Monitoring Technologies in Mechanical Systems*, 7th International Conference on Acoustical and Vibratory Surveillance Methods and Diagnostic Techniques (Surveillance 7), 29-30 October 2013, Chartres, France.

[27] A. Carcaterra *et al, A new theory of shock response in structural dynamics*, ICEDyn 2011- International Conference on structural Engineering Dynamics. Tavira. ISBN 978-989-96276-0-4.

[28] N. Roveri, A. Carcaterra, A. Akay, *Frequency intermittency and energy pumping by linear attachments*, Journal of Sound and Vibration, Available online 14 May 2014, http://dx.doi.org/10.1016/j.jsv.2014.04.003.